Mars 2020 Reconstructed Aerothermal Environments and Design Margins

Karl T. Edquist*
NASA Langley Research Center, Hampton, Virginia 23681

Milad Mahzari† Hannah S. Alpert‡
NASA Ames Research Center, Moffett Field, California 94035

The Mars 2020 aeroshell's thermal protection system was nearly identical to the Mars Science Laboratory system that successfully completed its mission for the Curiosity rover's landing in 2012. It was predicted that, like Mars Science Laboratory, the Mars 2020 heatshield would experience boundary layer transition and that the thermal protection system would provide sufficient material thickness margins against the aerothermal environments, even after adding radiative heating that was not included for Mars Science Laboratory. The Mars 2020 flight instrumentation suite included heatshield sensors similar to Mars Science Laboratory and new backshell measurements. A full set of surface pressure and in-depth temperature data were collected during atmospheric entry. This paper provides an initial analysis of the flight data and focuses on the reconstructed total surface heat flux inferred from the measured temperatures. Turbulent boundary layer conditions again were observed on the Mars 2020 heatshield, and the temperatures at all eleven heatshield and six backshell thermocouple in-depth sensor locations were well within system capabilities due to favorable entry conditions and conservative uncertainties. New computational fluid dynamics results on the reconstructed entry trajectory are compared to the measured surface pressures and reconstructed total heat fluxes. The predicted heatshield surface pressures at six locations match the data qualitatively and quantitatively well, as expected. Smooth-wall laminar heating predictions prior to boundary layer transition fall above the reconstructed heating on the heatshield. After the observed boundary layer transition time, total heat flux based on algebraic turbulence model calculations generally match the heat flux trends relative to one another. The convective heat flux was predicted to constitute the majority of the total heating. On the backshell, smooth-wall laminar total heat flux predictions generally exceed the reconstructed total heating at six locations. At each of these locations, it is estimated that radiative heating provided almost all of the total heating. The Mars 2020 as-flown aerothermal environments were well below the design levels for all measurement locations due to conservative design assumptions and a stressing design trajectory.

*Aerospace Engineer, Atmospheric Flight and Entry Systems Branch, Mail Stop 489, AIAA Associate Fellow, karl.t.edquist@nasa.gov.
†Aerospace Engineer, Entry Systems and Vehicle Development Branch, AIAA Member.
‡Aerospace Engineer, Analytical Mechanics Associates, Inc., AIAA Member.

Nomenclature

Symbols

a_w	speed of sound at wall	m/s
C_H	convective heat transfer coefficient	$kg/m^2/s$
h_w	enthalpy at wall	$J/kg-K$
$\bar{q}$	dynamic pressure, $\frac{1}{2}\rho_\infty V_\infty^2$	kPa
q_{conv}	hot-wall convective heat flux	W/cm^2
q_{rad}	radiative heat flux	W/cm^2
$Re_{cell,w}$	Reynolds number at wall cell, $\rho_w a_w \Delta h/\mu_w$	
T_w	wall temperature	K
T_∞	atmospheric temperature	K
V_∞	freestream velocity	m/s
α	angle of attack	deg
α_w	absorptivity	deg
Δh	height of wall grid cell	m
ϵ	emissivity	
μ_w	viscosity at wall	$kg/m^2/s$
ρ_w	density at wall	kg/m^3
ρ_∞	atmospheric density	kg/m^3
σ	Stefan's constant (5.67×10^{-8})	$W/m^2/K^4$

Acronyms

BET	Best Estimated Trajectory
BLT	Boundary Layer Transition
C-S	Cebeci-Smith algebraic turbulence model
CFD	Computational Fluid Dynamics
EDL	Entry, Descent, and Landing
EI	Atmospheric Entry Interface
HARA	High-Temperature Aerothermodynamic Radiation Algorithm
LAURA	Langley Aerothermodynamic Upwind Relaxation Algorithm
MEADS	MEDLI Entry Atmospheric Data System
MEDLI	Mars Entry, Descent, and Landing Instrumentation
MISP	MEDLI Integrated Sensor Plug
MPB	MEADS Pressure on Backshell
MPH	MEADS Pressure on Heatshield
MTB	MISP Thermal on Backshell
MTH	MISP Thermal on Heatshield
PICA	Phenolic Impregnated Carbon Ablator
PRT	Piezo Resistive Transducer
RTD	Resistance Temperature Detector
SLA	Super-Lightweight Ablator
TC	Thermocouple
TPS	Thermal Protection System
VRT	Variable Reluctance Transducer

I. Introduction

The Mars 2020 entry system successfully delivered the Perseverance rover to Jezero crater on the 18^{th} of February 2021. The hypersonic atmospheric entry phase of the entry, descent, and landing (EDL) sequence was executed using a rigid aeroshell and thermal protection system (TPS) that were almost identical versions of those used for the successful Mars Science Laboratory (MSL) Curiosity rover landing in 2012. The Mars Entry, Descent, and Landing Instrumentation (MEDLI) suite was added to the heatshield in order to measure aeroshell surface pressures and temperatures below the TPS surface.[1] The main purpose of MEDLI was to return high-quality engineering data that could be used to calibrate the accuracy of analytical design tools and improve analytical aerosciences design methods. The MEDLI system successfully collected the most comprehensive engineering data for any Mars lander mission to date. The MEDLI package was specifically added to the MSL heatshield because of this lack of data and because the MSL heatshield was expected to experience boundary layer transition (BLT) and turbulent convective heating during EDL. MEDLI successfully measured heatshield surface pressures at seven locations and in-depth temperatures at seven different locations, and provided the opportunity to directly assess TPS performance and predictive flowfield and thermal response models that were originally used for TPS design. The MEDLI data were used to confirm that the Phenolic Impregnated Carbon Ablator (PICA) heatshield material experienced BLT during entry. More importantly, the data showed that the PICA thermal response was as expected and that the as-flown material thickness determined through extensive pre-flight computational fluid dynamics (CFD) and thermal response modeling resulted in maximum TPS temperatures that were below allowable design limits.[2]

The Mars 2020 entry system was formulated to use the MSL aeroshell and TPS design with as few changes as possible. This design approach meant that the normal analysis cycle of determining the appropriate TPS material thicknesses through CFD analysis, thermal response modeling, and ground testing was not used for Mars 2020.[3] The MSL material thicknesses for PICA on the heatshield (1.25 inches), SLA-561V on the backshell (0.5 inches), and Acusil-II on the parachute cone (variable thicknesses) were unchanged for the Mars 2020 vehicle, with the exception of minor changes to the structure and TPS on the parachute cone lid. Consequently, the Mars 2020 pre-flight analysis was focused on determining whether the MSL TPS design would provide sufficient material thickness margins for the Mars 2020 entry aeroheating design environments. This approach was chosen in part to reduce development cost and schedule risks, but also because the convective heating environments predicted for Mars 2020 were expected to be less severe than what the MSL TPS experienced due to a lower entry speed at Mars arrival. Previous research[4] showed that one key missing element from the MSL entry aeroheating analysis was the contribution of shock layer radiation to the heatshield total heat flux experienced by the TPS, especially on the backshell. This erroneous omission was uncovered through improvements in shock layer radiation modeling and ground testing after the MSL entry vehicle was built. Although the MEDLI instrumentation did not directly measure shock layer radiation, it was strongly suspected to be the reason for differences between MSL post-flight CFD analysis and reconstructed total heat flux.[5] Consequently, whereas the MSL TPS design considered only convective heating, the Mars 2020 analysis also included radiative heat flux predictions.

There are two main reasons why the MSL TPS design provided sufficient margins for the Mars 2020 aeroheating environments, even after adding shock layer radiation. On the Mars 2020 heatshield TPS, convective heating was predicted to contribute most of the total heat flux, so adding a relatively small contribution from shock layer radiation did not result in total combined heat fluxes (convective plus radiative) that exceeded the convective-only heat fluxes for MSL. On the backshell TPS, radiative heating was predicted to be a much larger component of total heat flux, sometimes well over half the combined heating. Fortunately, analysis for Mars 2020 showed that the conservative uncertainties that were originally built into the MSL backshell's convective-only aeroheating environments were large enough to cover the addition of radiative heating at Mars 2020 conditions. The Mars 2020 flight instrumentation (MEDLI2) was included to provide a set of measurements on the heatshield similar to what MEDLI provided. More importantly, TPS measurements on the Mars 2020 backshell were added to improve our understanding of aeroheating environments in a wake flowfield where shock layer radiation was expected to contribute the majority of the total heating in most locations. Analysis of the flight data includes a full description of the data products,[6] trajectory[7] and atmosphere reconstruction,[8] aeroshell aerodynamic performance,[9] and entry simulation assessment.[10] Detailed analysis of the aerothermal flight data includes updating analytical models for TPS material response

analysis,[11] estimating surface heating using measurements of temperature in the TPS materials,[12] analyzing directly-measured surface heating on the aeroshell aftbody,[13] and observations on boundary layer transition on the heatshield.[14]

The material presented here includes an initial analysis of the flight data products and assessment of the aeroheating margins and design tools at reconstructed entry conditions. More in-depth analysis of the flight data has begun within the NASA Space Technology Mission Directorate, and results from that research will be published over the next few years. This longer term research will involve detailed investigations of the entire MEDLI2 dataset and will include expanded analysis of the atmosphere reconstruction, additional TPS material and aeroheating testing, and computational analysis with more advanced tools to address deficiencies in current methods and to explore reducing design uncertainties. The paper is organized as follows: an overview of the MEDLI2 instrumentation in Section II, a summary of the pressure and temperature data for the Heatshield in Section III and Backshell in Section IV, the reconstructed total heat flux in Section V, and new smooth-wall CFD calculations at reconstructed entry conditions in Section VI. The section also includes a comparison between as-flown, as-predicted, and design aeroheating environments, which shows that all aerothermal measurement locations experienced total heating that was below the TPS design environments.

II. MEDLI2 Flight Instrumentation

Figure 1, Figure 2, and Table 1 summarize the MEDLI2 instrumentation sensor details and locations on the aeroshell. Surface pressure was measured directly at seven heatshield locations (MPH01 through MPH07). The MPH01 sensor was designed to capture the entire hypersonic pressure pulse and the remaining sensors were designed to better measure lower pressures later in the EDL sequence prior to parachute deployment. All pressure data were used to reconstruct the entry trajectory, specifically the entry vehicle attitude and atmospheric density profile.[7] At eleven other heatshield locations (MTH01 through MTH11), temperatures were measured using thermocouples (TCs) embedded below the TPS surface, with some locations having multiple measurement depths. At each TC plug location, the measured temperatures were used to determine material performance and to reconstruct the total heat flux at the TPS surface. The heatshield thermal plug locations were selected to observe the expected progression of BLT over the heatshield during entry, especially on the leeside ($X_{sc} < 0$ in Figure 1). The MSL aeroshell did not have any measurements on its backshell or parachute cone. For Mars 2020, pressure was measured (MPB01) at one backshell location. New backshell aerothermal measurements included in-depth temperature measurements using TCs (MTB01 through MTB06), direct total heat flux measurements (MTB07 and MTB08), and a radiometer (MTB09) to measure the radiative component of heating. No instrumentation was installed on the parachute cone. The MEDLI2 instrumentation and various analyses using the flight data are described in detail elsewhere.[6–8,10–14]

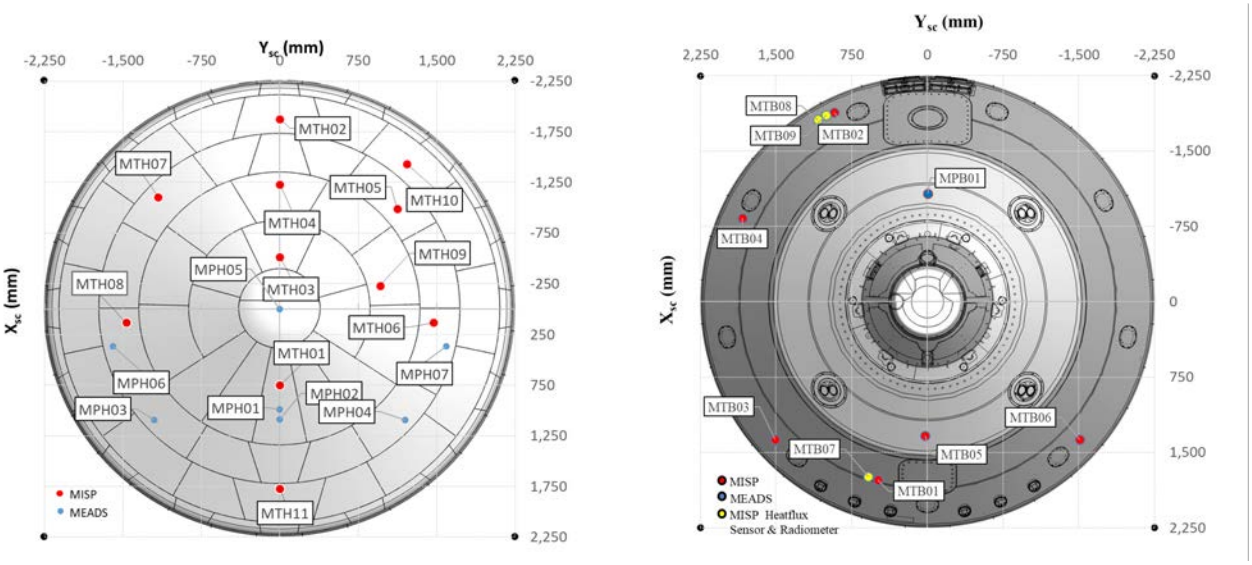

(a) Heatshield

(b) Backshell and parachute cone

Figure 1. MEDLI2 instrumentation locations.

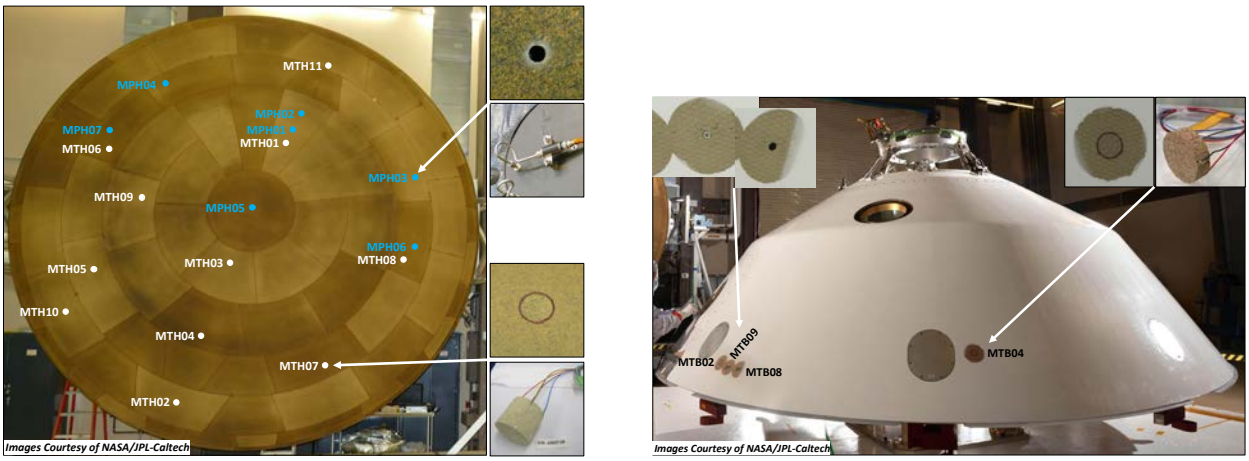

(a) Heatshield

(b) Backshell (with white paint over SLA-561V)

Figure 2. Flight hardware.

Table 1. MEDLI2 instrumentation details.

Sensor Name	Type	Data rate(s) (Hz)	Notes	Y_{sc} (mm)	X_{sc} (mm)
MPH01	HPT	8*, 1	MEDLI spare	0	-1000
MPH02	SPT	8*, 1	PRT	0	-1089
MPH03	SPT	8*, 1	PRT	-1200	-1092
MPH04	SPT	8*, 1	PRT	1200	-1092
MPH05	SPT	8*, 1	PRT	0	0
MPH06	SPT	8*, 1	PRT	-1593	-365
MPH07	SPT	8*, 1	PRT	1593	-365
MTH01	PICA plug	8, 4, 1	TCs at 1.905, 5.08, 10.16 mm	0	-749
MTH02	PICA plug	8, 4, 1	TCs at 1.905, 5.08, 10.16 mm	0	2002
MTH03	PICA plug	8, 4, 1	TCs at 1.905, 5.08, 10.16 mm	0	515
MTH04	PICA plug	8	TC at 2.54 mm	0	1232
MTH05	PICA plug	8	TC at 2.54 mm	1122	990
MTH06	PICA plug	8	TC at 2.54 mm	1469	-129
MTH07	PICA plug	8	TC at 2.54 mm	-1164	1105
MTH08	PICA plug	8	TC at 2.54 mm	-1469	-129
MTH09	PICA plug	8	TC at 2.54 mm	959	228
MTH10	PICA plug	8	TC at 2.54 mm	1246	1567
MTH11	PICA plug	8	TC at 2.54 mm	0	-1773
MPB01	LPT	8*	VRT with external RTD	-6	1076
MTB01	SLA-561V plug	8, 4	TCs at 2.54, 6.35 mm	491	-1772
MTB02	SLA-561V plug	8	TC at 2.54 mm	921	1882
MTB03	SLA-561V plug	8	TC at 2.54 mm	1509	-1373
MTB04	SLA-561V plug	8	TC at 2.54 mm	1834	830
MTB05	SLA-561V plug	8	TC at 2.54 mm	23	-1331
MTB06	SLA-561V plug	8	TC at 2.54 mm	-1509	-1373
MTB07	Heat flux sensor	16, 1	S-B with TC	586	-1742
MTB08	Heat flux sensor	16, 1	S-B with TC	1002	1855
MTB09	Radiometer	16, 1	Sapphire window over S-B with TC	1083	1810

HPT: Hypersonic pressure transducer

LPT: Low pressure transducer

PRT: Piezo Resistive Transducer with internal temperature sensor

RTD: Resistance Temperature Detector

S-B: Schmidt-Boelter gage

SPT: Supersonic pressure transducer

TC: Thermocouple

VRT: Variable Reluctance Transducer

III. Heatshield Data and Boundary Layer Transition

Figure 3 shows the heatshield pressure data collected during entry. The figure inset shows the measurement locations and predicted streamlines at peak heating time on the as-flown trajectory when the aeroshell was at an angle of attack near 16 degrees. All sensors returned a complete set of data with no dropouts and minimal indication of pre-entry shifts. The MPH01 stagnation pressure captures the full extent of the pressure pulse, which was needed to help reconstruct the full entry trajectory. The peak value was reached

87.48 seconds after entry interface. The remaining heatshield sensors were calibrated to better capture pressure magnitudes at low supersonic conditions, thus the clipped levels between about 65 and 125 seconds. All pressure sensor data were used to help reconstruct the entry trajectory, atmosphere conditions, and entry vehicle aerodynamicsREF.

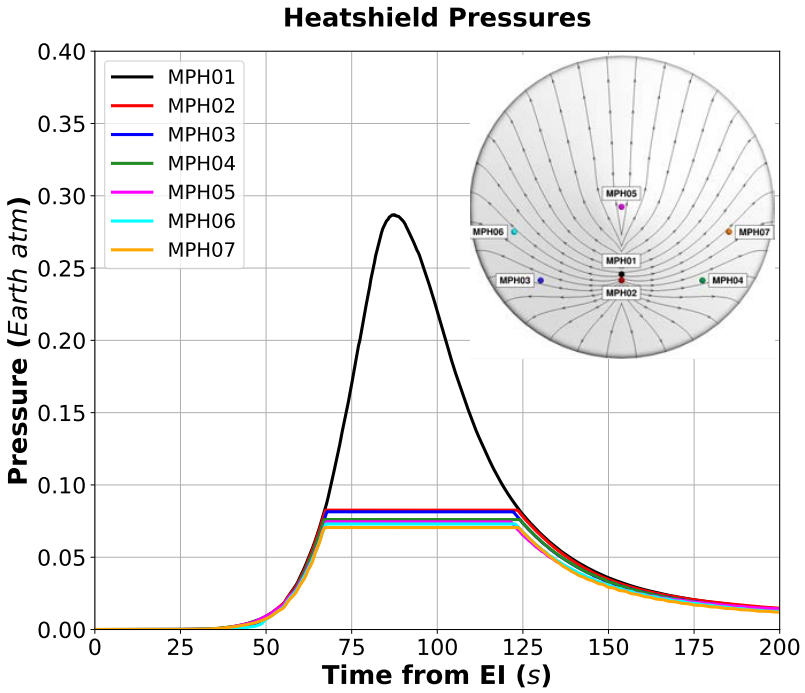

Figure 3. Measured heatshield pressures.

The expectation was that heatshield BLT would occur early enough in the Mars 2020 entry trajectory that peak heating would be under turbulent conditions. There was no pre-flight analysis specifically aimed at predicting the exact timing of BLT, so the TPS was designed to withstand environments based on turbulent calculations along the entire entry trajectory. Figure 4 shows the measured temperatures at the TC locations closest to the surface. Like MSL, none of the data channels dropped out, which means that the PICA recession never reached the TC depths. The highest temperatures were observed at MPH02 and MPH03, in part because the top-most TCs were closer to the surface, but also because turbulent heating conditions were suspected based on slope discontinuities in the temperature curves between 70 and 80 seconds. As was shown in the post-flight MSL analysis, the times at which BLT occured are best detected by examining the time-derivative of temperature (Figure 5). The figure shows that nine of the eleven thermal plug locations experienced BLT as indicated by the rapid increase in the temperature time-derivative. The only two locations where BLT is not apparent (MTH01 and MTH11) are in the stagnation area where BLT was not expected. The MTH02 plug experienced BLT first, followed by locations gradually towards the heatshield nose and locations closer to the shoulder on each side. Table 2 shows the approximate BLT onset times at each plug location, in order of occurrence, based on the initial slope change in the temperature curves.

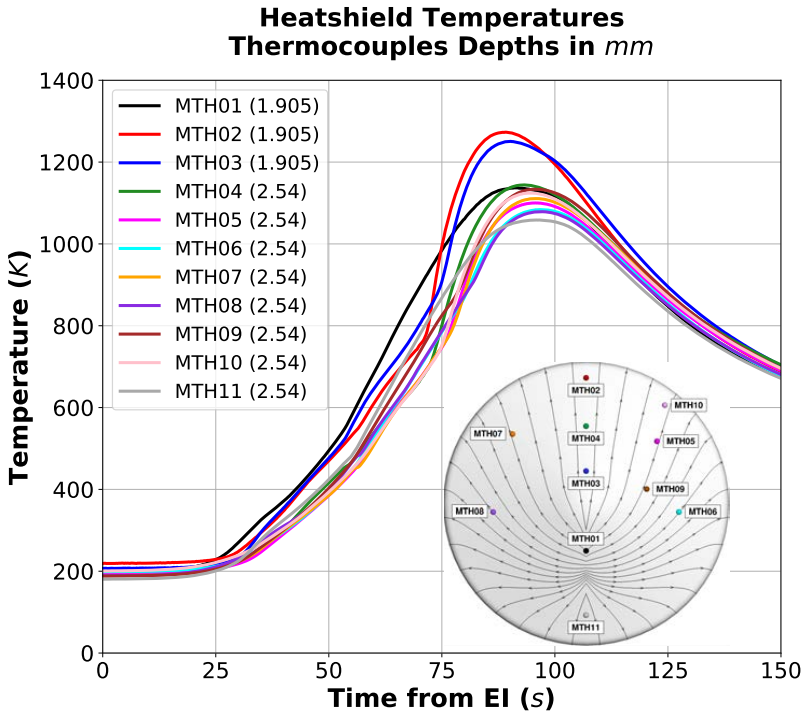

Figure 4. Measured heatshield temperatures at shallowest thermocouples.

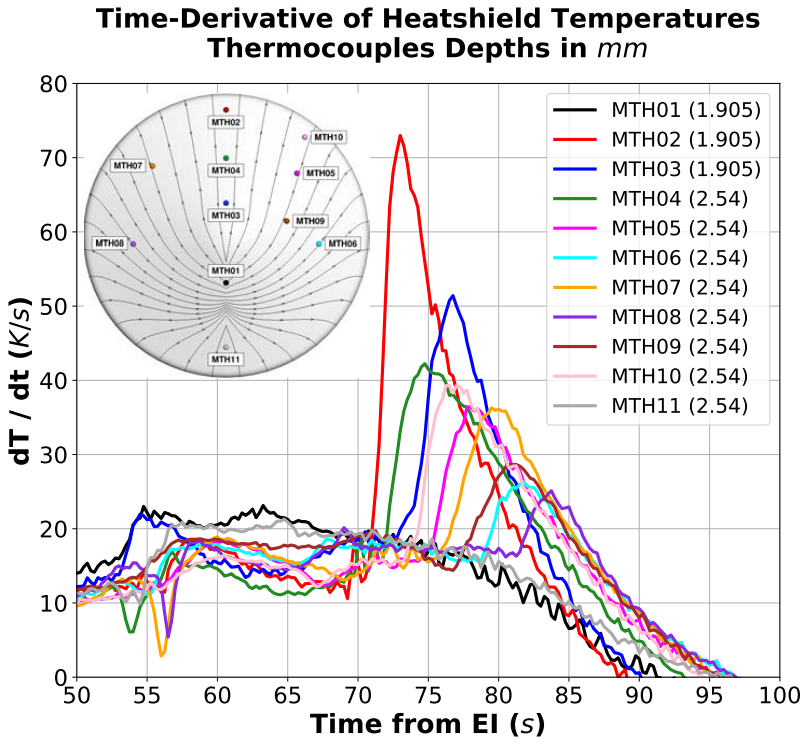

Figure 5. Time-derivative of heatshield temperatures at shallowest thermocouples.

Table 2. Heatshield estimated BLT onset times based on near-surface temperature time-derivative.

Location	BLT onset time from EI (s)
MTH02	71
MTH04	72
MTH03	73
MTH10	74
MTH05	75
MTH07	76
MTH09	77
MTH06	79
MTH08	81
MTH01	N/A
MTH11	N/A

IV. Backshell Data

Figure 6 shows the backshell pressure data collected at the MPB01 location during entry. Based on pre-flight CFD calculations, this sensor was expected to always be in separated wake flow during EDL. The sensor returned a complete set of data with no dropouts and minimal indication of pre-entry shifts. The pressure magnitudes were less than 1% of the pressures measured on the heatshield. Peak pressure occurred at 94.73 seconds after entry interface, or about seven seconds after the heatshield MPH01 peak. The temperatures and time-derivatives at the six plug locations are shown in Figure 7 and Figure 8. The highest measured temperature occurred at the MTB02 locations, where the flow likely was separated. There is no obvious indication of BLT at any of the plug locations based on the time-derivative of temperature.

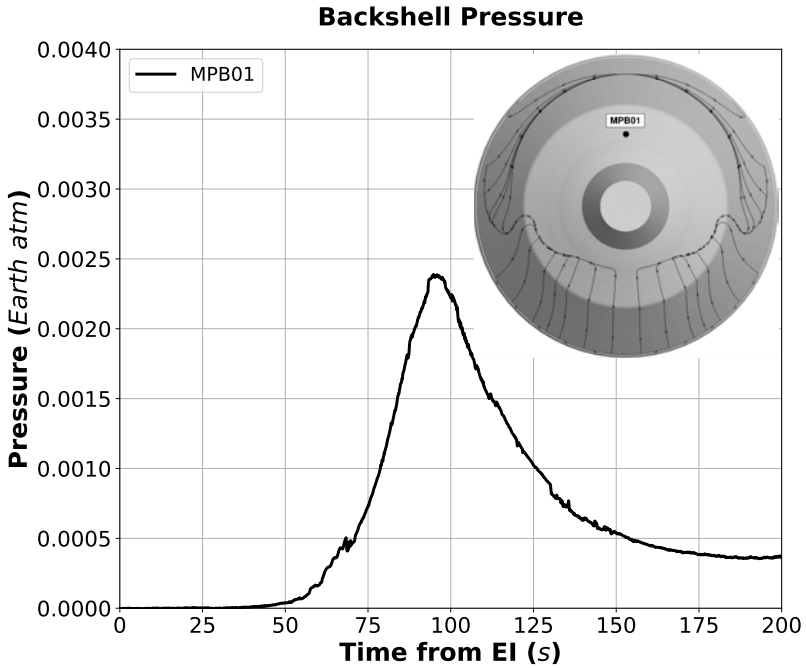

Figure 6. Measured backshell pressure.

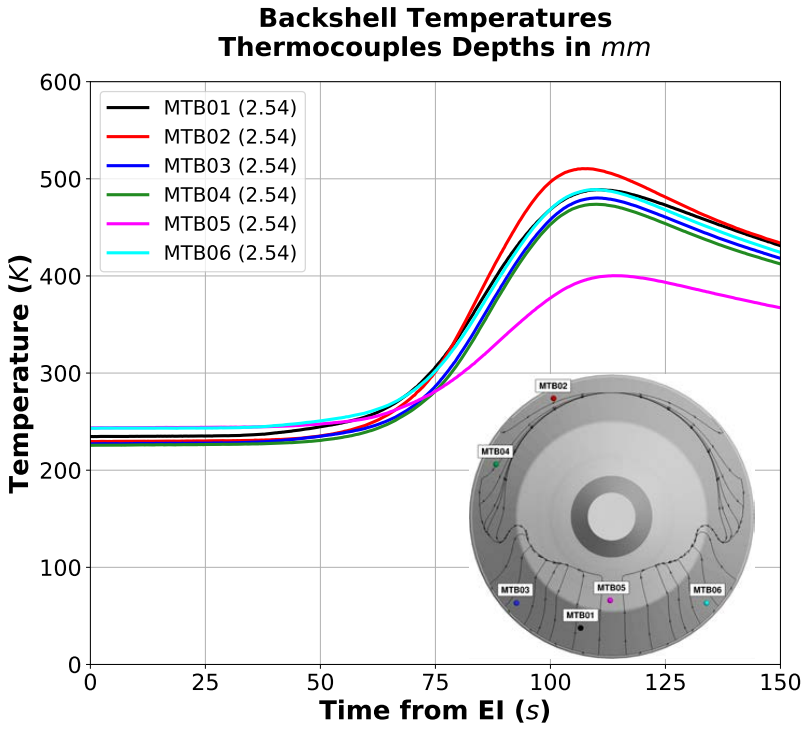

Figure 7. Measured backshell temperatures at shallowest thermocouples.

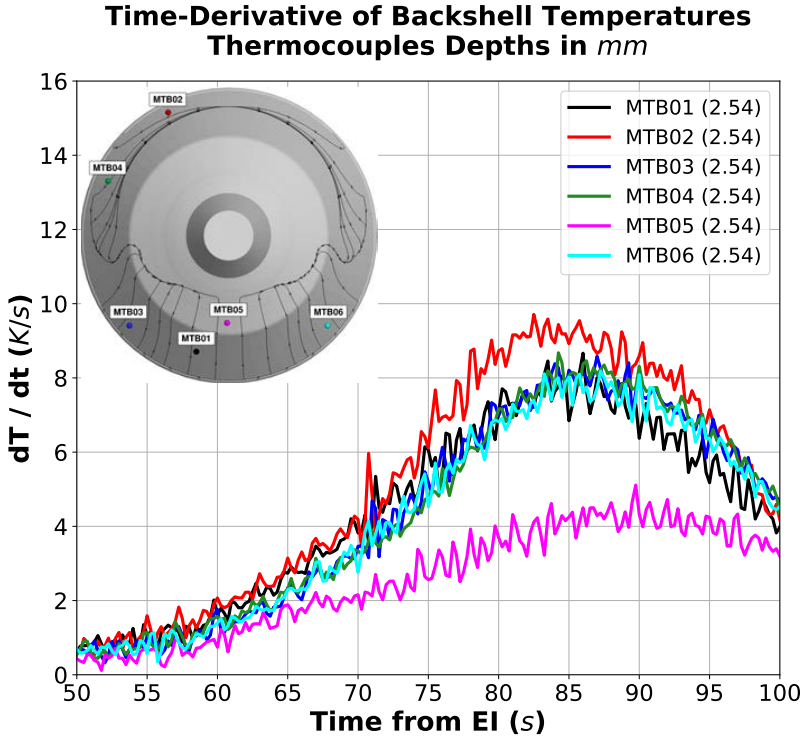

Figure 8. Time-derivative of backshell temperatures at shallowest thermocouples.

V. Inverse Reconstruction of Total Heating

Reconstructing the total surface heating is achieved by inversely solving the heat conduction through the material layer above the thermocouples where temperature was measured. This inverse method requires solving the surface energy balance using a thermal response model, which in this case is the Fully-Implicit Ablation and Thermal (FIAT) analysis code.[15] The reconstruction is numerically accomplished by iteratively optimizing surface heating such that the difference between FIAT temperature predictions and the measured temperature data are minimized. Results from the inverse method are subject to uncertainties in the material properties, ablative modeling parameters, and amount of recession. The typical FIAT ablative response model includes all energy terms: the incoming heating environment, the material response, re-radiation, and conduction into the material. This surface energy balance[16] for an ablating material is:

$$C_H(H_r - h_w) + \alpha_w q_{rad} + \dot{m}_g h_g + \dot{m}_c h_c - (\dot{m}_g + \dot{m}_c)h_w = \sigma\epsilon(T_w^4 - T_\infty^4) + q_{cond} \quad (1)$$

The first and second terms are the incoming heat transfer: convective heat transfer coefficient (C_H), recovery (H_r) and wall enthalpies (h_w), and absorptivity times radiative heating ($\alpha_w q_{rad}$). The remaining terms on the left-hand side represent the ablative material response; $\dot{m}$ and h are mass flow rate and enthalpy, where the subscript g represents the pyrolysis gases (blowing) and the subscript c represents the char material (recession). The right-hand side includes re-radiation and conduction; the latter term is directly related to the measured in-depth temperatures. Convective radiative heating cannot be individually extracted from the TC data since they have similar effects on in-depth temperature. Therefore, the results presented in this paper represent the sum of convective plus absorbed radiative heat flux ($q_{conv} + \alpha_w q_{rad}$), including pyrolysis gas blowing.[12]

One complicating factor in reconstructing the Mars 2020 heatshield aeroheating is the existence of a thin NuSil coating that was sprayed over the PICA material in order to satisfy planetary protection requirements. The coating has been observed in testing to inhibit PICA recession, which is consistent with the near-surface TCs surviving entry. At this time, the FIAT model for PICA with NuSil still is being developed with the help of additional ground testing. Therefore, the reconstruction to date is based on a slightly different version of the energy balance equation with recession and the NuSil thermal response omitted.[12] The inverse results shown here represent the current state of the analysis for the heatshield and backshell thermal plug locations, but should not be considered final.

The reconstructed heating for the eleven heatshield thermal plug locations is shown in Figure 9. Early in the entry trajectory and prior to BLT, the highest heating occurred at the two locations in the stagnation area, MTH01 and MTH11. After BLT, the thermal plugs on the opposite side of the stagnation area (MTH02 and MTH04) experienced the highest heating under turbulent conditions. The MTH02 plug was situated near the location of maximum predicted turbulent heat flux. The reason for the spike in the MTH02 heating curve is not known at this time. Possible causes include a transitional overshoot prior to reaching turbulent conditions, and a unique TC response to the rapid temperature rise during BLT. Two of the symmetric plug locations, MTH06 and MTH08, had similar heating profiles, which is indicative of a negligible angle of sideslip. Three of the thermal plugs (MT09, MTH05, and MTH10) were purposely placed to approximately follow the same predicted surface streamline. The trend is that the turbulent heating along that streamline increases with running length away from the stagnation area, as would be expected.

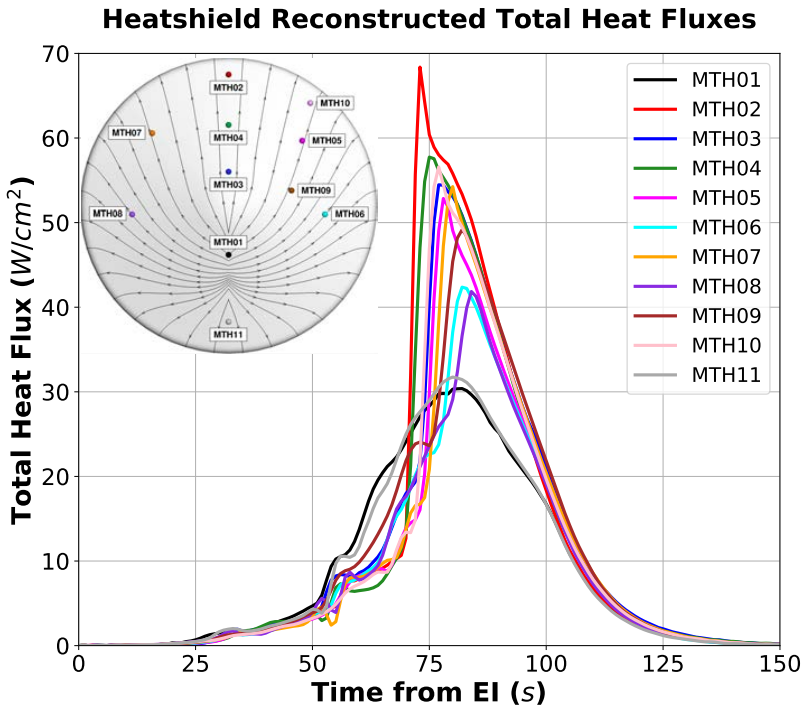

Figure 9. Reconstructed total heat fluxes on the heatshield.

The reconstructed total surface heating at the six backshell thermal plug locations is shown in Figure 10. The plug locations on the windward side (bottom half) were expected to be in attached flow during entry. The highest heating occurred at the MTB02 location, which was expected to be in separated flow. Data from the two nearby direct heat flux sensors (MTB07 and MTB08) and radiometer (MTB09) eventually will help determine the proportions of convective and radiative heating. The double peaks in the total heat flux, especially apparent at MTH02, may be the result of separate convective and radiative maxima, but the reason will be investigated as part of detailed analysis.

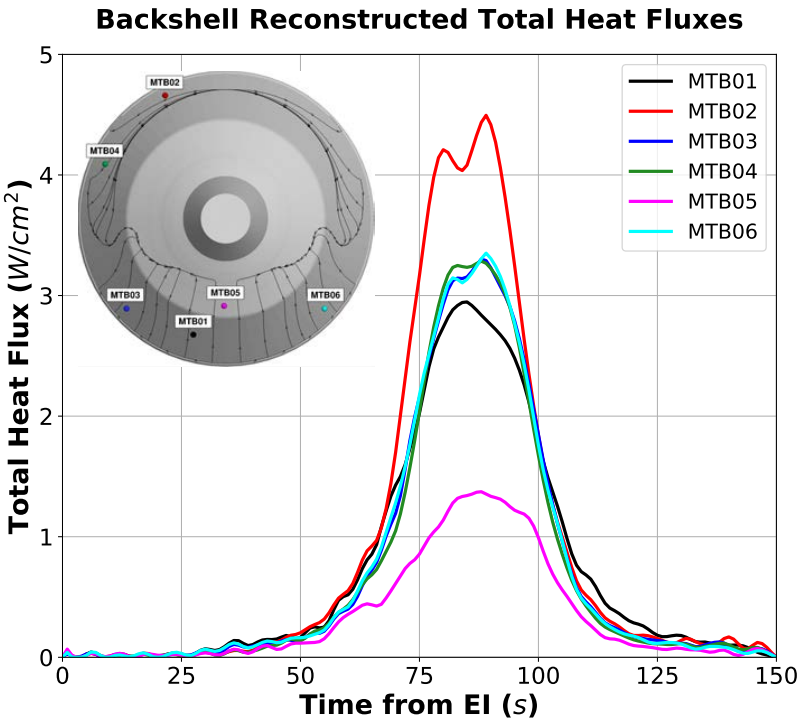

Figure 10. Reconstructed total heat fluxes on the backshell.

VI. Computational Flowfield Results Compared to Flight Data Products

Conditions along the as-flown entry trajectory were required in order to make comparisons between post-flight CFD analysis and the MEDLI2 data products: pressure and reconstructed total heat flux. The reconstructed best estimated trajectory (BET) is based on a combination of on-board GN&C measurements and the MEDLI2 heatshield pressure data.[7] Figure 11 and Table 3 show the BET compared to the MSL BET and the two Mars 2020 TPS design trajectories: shallow entry flight angle (19-TPS-01) and steep (19-TPS-02). The as-flown Mars 2020 entry trajectory had a slightly lower entry speed compared to the two TPS design trajectories, as expected. This difference led to an as-flown trajectory that resulted in slightly lower total heating based on stagnation point correlations.[17] The design trajectories were not selected based on a specific landing location and day of arrival, but rather on the highest entry speed possible within a range of latitudes inside the launch-arrival window. The MSL peak dynamic pressure is slightly higher than what the Mars 2020 entry vehicle experienced due to having a higher entry speed. The Mars 2020 entry vehicle nominally was designed to fly at the same angle of attack that MSL, which was confirmed in the reconstruction. The MSL and Mars 2020 reconstructed atmospheric density profiles have differences that are expected due to the unique landing site locations and arrival times.

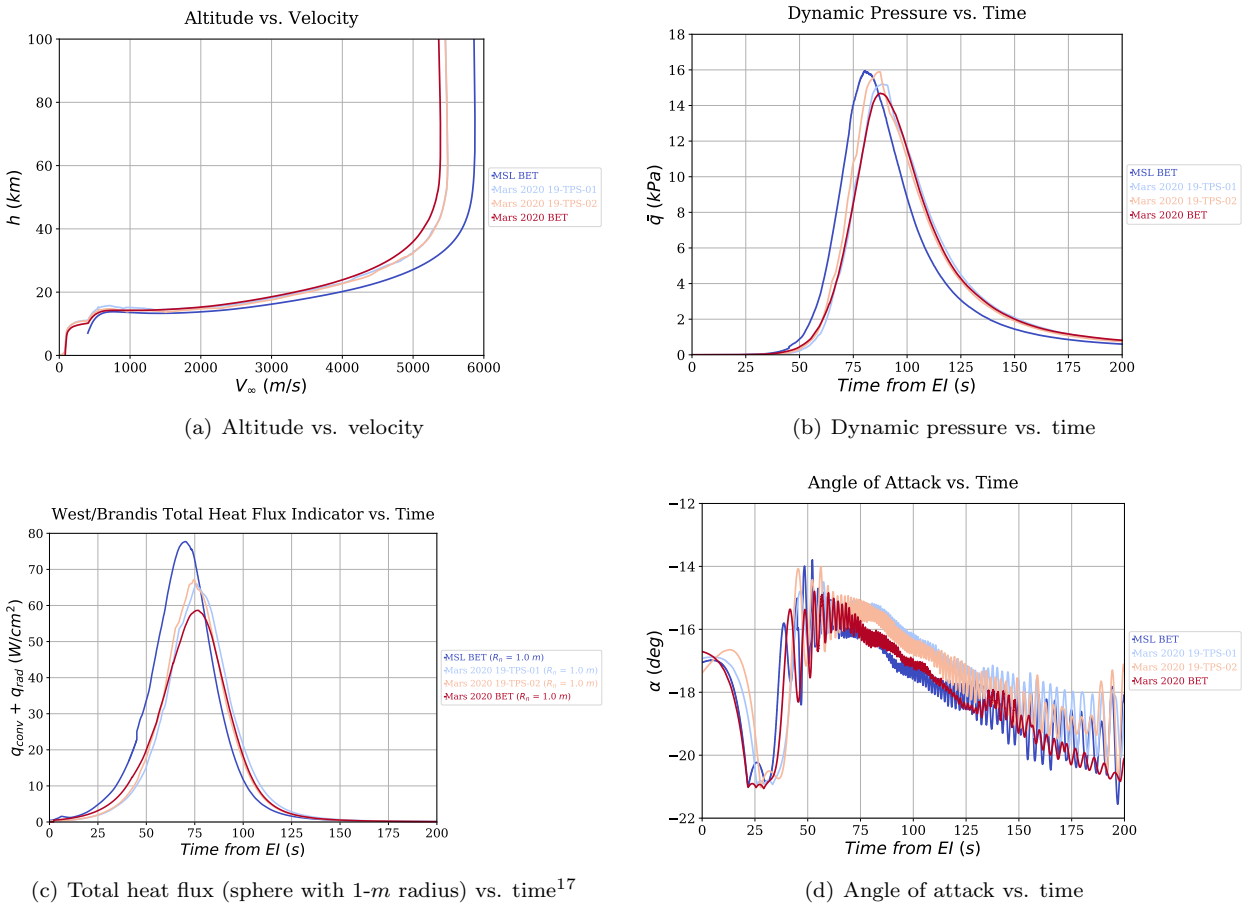

(a) Altitude vs. velocity

(b) Dynamic pressure vs. time

(c) Total heat flux (sphere with 1-m radius) vs. time[17]

(d) Angle of attack vs. time

Figure 11. Mars 2020 BET compared to MSL BET and Mars 2020 TPS design trajectories.

Table 3. Mars 2020 BET compared to MSL BET and Mars 2020 TPS design trajectories.

	MSL BET	Mars 2020 19-TPS-01	Mars 2020 19-TPS-02	Mars 2020 BET
Entry mass (kg)	3153	3436	3436	3369
Entry speed, (m/s)	5845	5428	5428	5334
Entry flight path angle (deg)	-16.12	-15.2	-15.56	-15.5
Peak dynamic pressure (Pa)	15,915	15,197	15,891	14,685

Conditions along the BET were selected for new CFD analysis to compare against the measured pressures and reconstructed total heat fluxes. The heat fluxes are shown only for locations where the in-depth TPS temperatures were measured. At this time, no comparisons have been made against the direct heat flux (MTB07 and MTB08) or radiometer (MTB09) measurements on the backshell. The same tools that were used for pre-flight aeroheating analysis were used at BET conditions: the *Langley Aerothermodynamic Upwind Relaxation Algorithm*[18] (LAURA) flowfield solver and the *High-Temperature Aerothermodynamic Radiation Algorithm*[19] (HARA) radiation code. LAURA provides surface pressure and convective heat flux, and HARA provides radiative heat flux. The LAURA calculations shown here assume a *fully-catalytic* surface model[20] (including the recombination of CO_2 and CO at the TPS surface), whereas the design environments assumed a more conservative *super-catalytic* surface (full recombination of all species to their freestream mass fractions). The fully-catalytic conditions are believed to better represent the gas-surface interactions at the TPS surface during flight. Since there is no indication of significant recession at any of the heatshield

thermal plugs, no roughness augmentation effects are applied to the LAURA turbulent convective heating. There is ongoing analysis to better refine the inverse heating estimation uncertainties and the raw data products where heat flux was directly measured. Table 4 shows the conditions selected for analysis.

Table 4. BET conditions for LAURA/HARA analysis.

Time from EI (s)	Altitude (km)	V_∞ (m/s)	ρ_∞ (kg/m^3)	T_∞ (K)	α (deg)	M_∞	$\bar{q}$ (kPa)
38.278	75.15	5385.7	5.175e-06	148.2	18.00	27.72	0.08
45.273	66.17	5387.8	1.564e-05	153.5	18.27	27.25	0.23
54.488	54.76	5368.3	5.762e-05	162.5	16.58	26.39	0.83
60.727	47.37	5299.9	1.408e-04	160.0	15.87	26.26	1.98
69.147	38.02	5079.6	3.898e-04	169.7	15.77	24.43	5.03
76.762[a]	30.43	4681.4	8.790e-04	174.9	16.42	22.18	9.63
83.037	25.12	4165.2	1.554e-03	176.7	16.43	19.64	13.48
87.552[b]	22.03	3716.7	2.103e-03	182.0	16.67	17.26	14.53
89.822	20.79	3488.4	2.364e-03	184.6	16.47	16.09	14.38
95.382	18.37	2961.4	2.980e-03	188.1	17.03	13.53	13.07
102.492	16.31	2396.2	3.607e-03	191.6	17.24	10.85	10.36
108.117	15.38	2048.6	3.910e-03	194.1	17.42	9.21	8.21
115.317	14.76	1710.0	4.146e-03	194.6	17.93	7.68	6.06
130.002	14.30	1263.5	4.396e-03	192.2	18.58	5.71	3.51

[a] Estimated peak stagnation point heat flux

[b] Peak dynamic pressure

Laminar and turbulent LAURA solutions were run at each trajectory condition in order to compare results against reconstructed total heating before and after BLT. The LAURA solutions were run in steady-state mode until the surface pressures and convective heat fluxes in the attached flow areas (entire heatshield and part of the backshell) changed minimally over several thousand iterations after the grid was adapted multiple times to the bow shock and near-surface regions. The calculations were then continued time-accurate until the running-average of backshell pressure and convective heating reached a relatively constant value over several thousand iterations. This extra step only was needed for the predicted environments on the backshell. The LAURA solutions were run with an 8-species gas (CO_2, N_2, O_2, NO, C, N, O) in chemical and thermal non-equilibrium. The Baldwin-Lomax algebraic turbulence model was used for TPS design analysis, but the current solutions are based on the Cebeci-Smith algebraic model. At most conditions, either perfect gas or chemically-reacting, the two algebraic models gives similar heating results for attached flow. However, recently it has been found that the Baldwin-Lomax model generates excessive turbulent viscosity at Mars entry conditions near peak heating and peak dynamic pressure. The Cebeci-Smith model does not generate such high viscosity and thus the results shown here were generated with that model. The final LAURA flowfields at each trajectory time were used to initiate decoupled HARA calculations of the radiative heat transfer. A ray-tracing approach[21] was used in HARA in which all lines-of-sight between the surface grid points and outer grid boundary are considered in the radiation calculations; the ray-tracing option gives the most accurate radiation predictions, especially for the backshell and parachute cone.

Figure 12 shows the computational surface grid and a sample adapted grid in the symmetry plane; one-quarter of the surface cells used are shown. A 92-block point-matched grid with 256 cells on the surface in each block was built on the as-designed TPS surface. The grid surface omitted minor details that were present on the aeroshell outer mold line, such as small gaps and steps, fasteners, antenna protrusions on the parachute cone, and detailed geometries of the installed MEDLI2 instrumentation. These details were not included in the grids used in pre-launch calculations because they did not impact aeroheating design environments for the heatshield and backshell TPS materials. The volume grid was constructed with 128 cells between the surface and outer boundaries. A built-in LAURA grid adaption capability was used to

distribute cells between the surface and outer boundaries. The cell height at the surface was governed using a cell-Reynolds number ($Re_{cell,w}=\rho_w a_w \Delta h/\mu_w$) near unity; ρ_w, a_w, Δh, and μ_w are density, speed of sound, cell height, and dynamic viscosity, respectively, in the cell bordering the surface. The grid outer boundary was automatically adjusted so that the majority of the grid cells were inside the shock layer and the grid was clustered at the shock front.

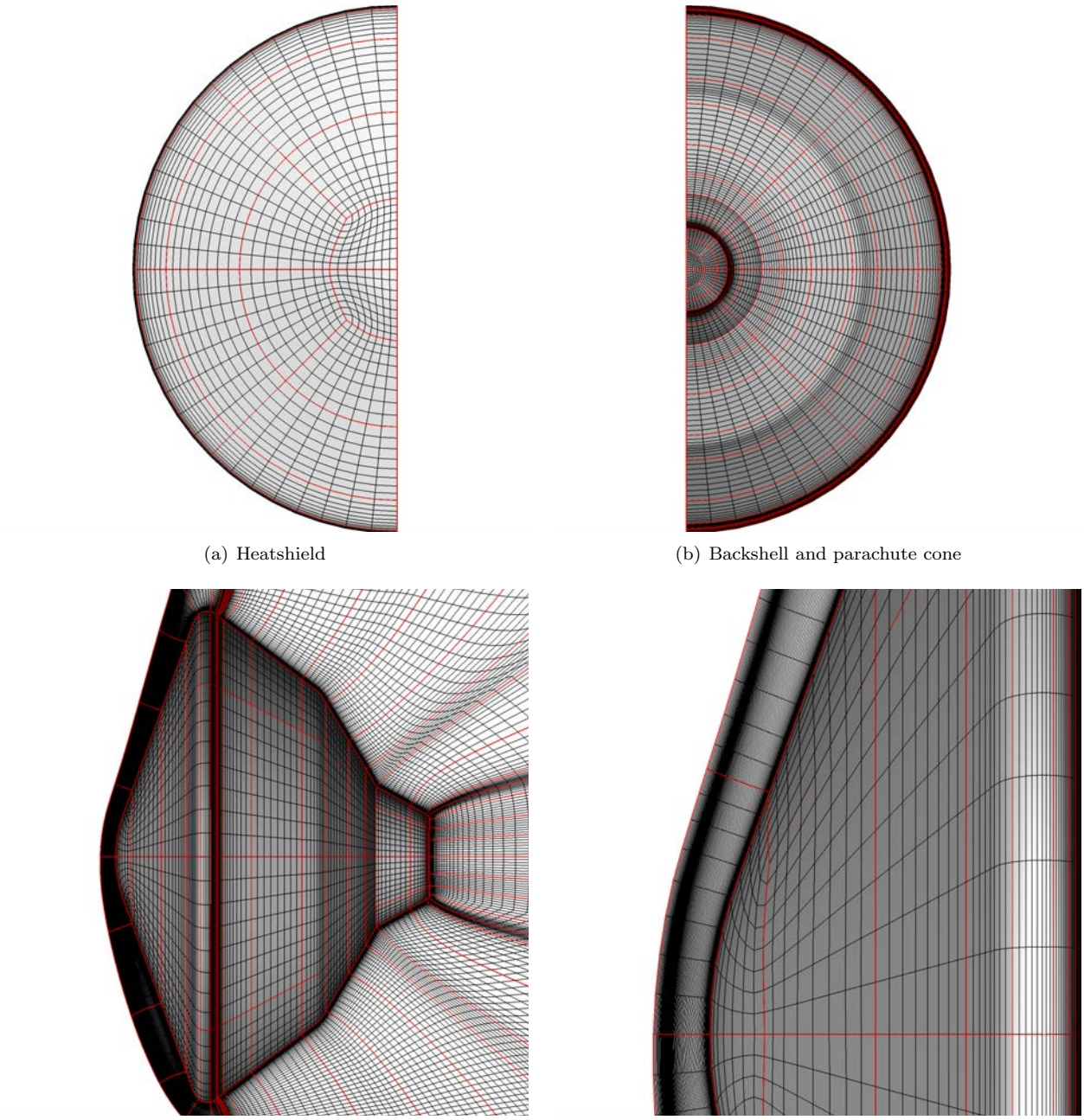

(a) Heatshield

(b) Backshell and parachute cone

(c) Symmetry plane.

(d) Grid adapted to shock and boundary layer

Figure 12. LAURA/HARA **grid with one-quarter of the surface cells shown.**

Results from the LAURA/HARA calculations at the trajectory time 76.762 seconds after entry interface are shown in Figure 13. This time is estimated for peak stagnation point heating. At the reconstructed angle of attack (16.42 degrees), the stagnation point sits on the heatshield conical surface ($X_{sc} > 0$). At this point in the trajectory, the convective heat flux on the heatshield is predicted to be as much as an order of magni-

tude higher than the radiative heating. The peak turbulent convective heating also is predicted to be on the side opposite from the stagnation point near the MTH02 thermal plug location. On the backshell, most of the windward side ($X_{sc} > 0$) is predicted to be in attached flow with higher convective heating compared to other areas. The radiative heating is not affected by whether the flow is predicted to be attached. In fact, the radiative heat flux at this time in the trajectory is predicted to be highest near the leeward shoulder ($X_{sc} < 0$) where the MTB02 thermal plug is located. This location has a direct line of sight to the thickest part of the bow shock in front of the heatshield and the high temperatures at the shock front make up most of the incoming radiation.

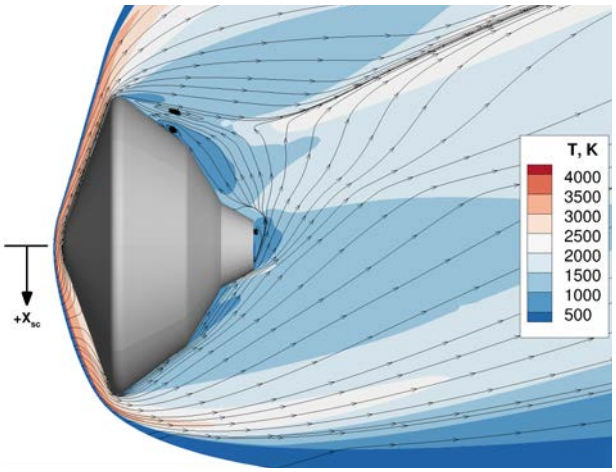

(a) Temperature

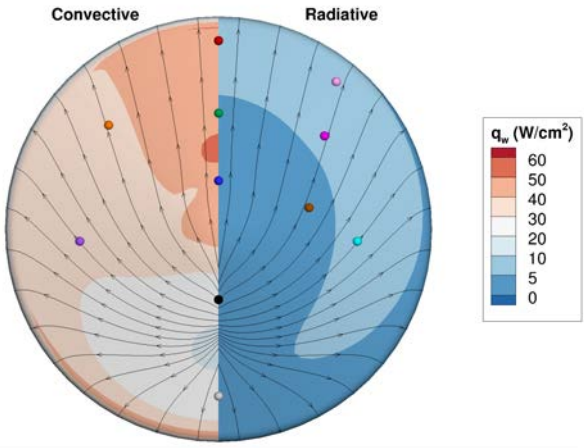

(b) Heatshield turbulent convective and radiative heat flux

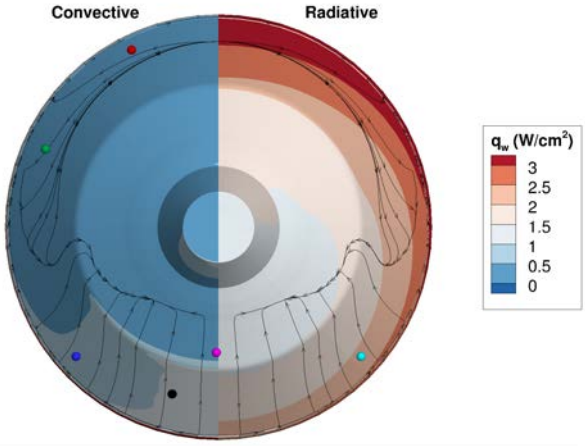

(c) Backshell and parachute cone laminar convective and radiative heat flux

Figure 13. Results from LAURA/HARA calculations at $t = 76.762$ *sec*.

Figure 14 shows comparisons between the pressure data and LAURA laminar predictions on the BET. As expected, LAURA predicts well the qualitative and quantitative pressure profiles at MPH01, where the measured pressure reached peak value 87.48 seconds after atmospheric entry interface (EI). The LAURA maximum pressure is within 3% of the measured peak and the predicted peak time is less than 0.3 seconds from the measured time. The BET used for the CFD is based on a combination of MEDLI2 pressure and inertial measurements. If the CFD had been run on a trajectory based solely on the heatshield pressure data, the CFD differences observed in heatshield pressure likely would be smaller. At the remaining supersonic pressure transducer locations, the LAURA pressures agree similarly with the data before and after sensor saturation.

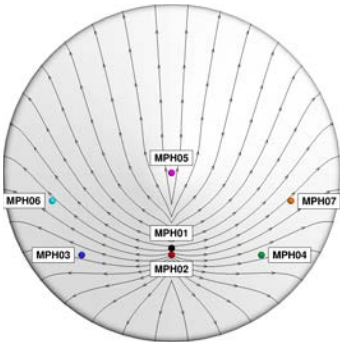

(a) Measurement locations and representative surface streamlines

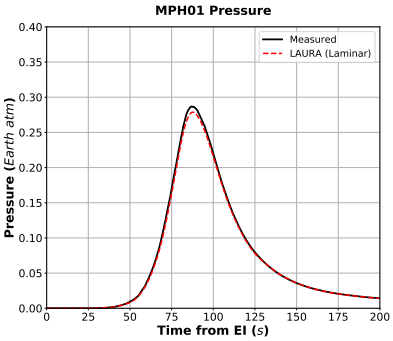

(b) MPH01

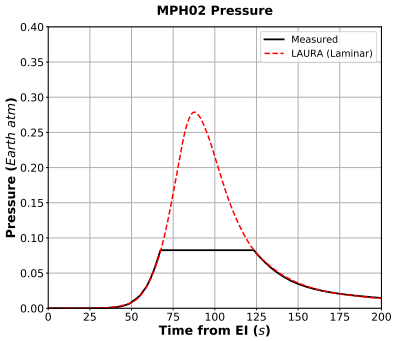

(c) MPH02

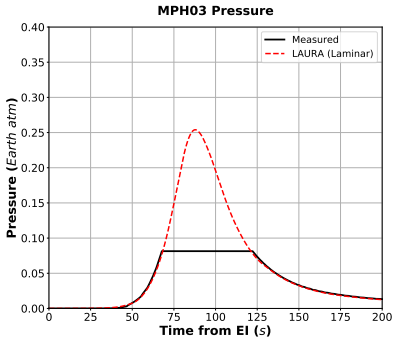

(d) MPH03

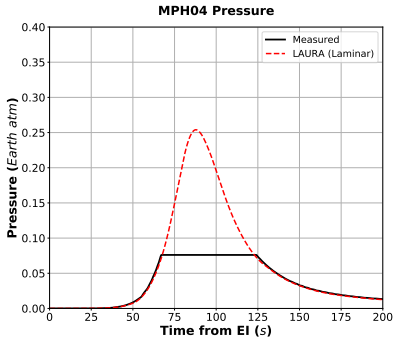

(e) MPH04

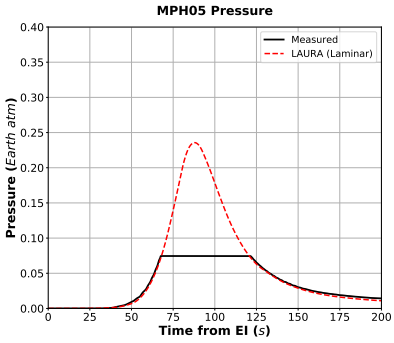

(f) MPH05

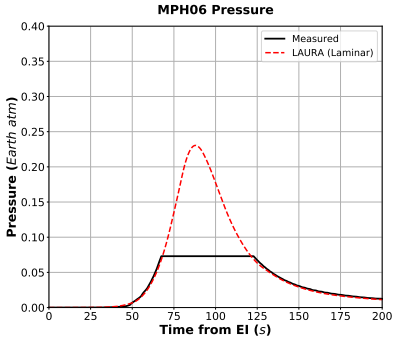

(g) MPH06

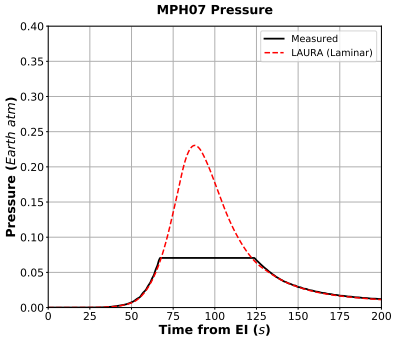

(h) MPH07

Figure 14. Measured heatshield pressures compared to LAURA laminar results.

Figure 15 shows the reconstructed heat fluxes compared to laminar and turbulent LAURA convective heat fluxes plus HARA radiative heat flux. The reconstruction results assumed no PICA recession as supported by the TC data closest to the surface. The reconstruction curves show the ±95% confidence intervals calculated using a Monte-Carlo approach that included uncertainties in thermocouple depths and PICA material properties, among others. It should be noted that the comparison of CFD-based and reconstructed heat fluxes is an approximate comparison, due to different assumptions in the CFD and thermal response, such as gas-surface reactions, pyrolysis gas blowing, and surface temperature. The LAURA calculations used a wall temperature in *radiative-equilibrium* ($q_{conv} = \sigma\epsilon T^4$) as a numerical boundary condition. Thus, the wall temperature in the LAURA simulation does not equal the reconstructed wall temperature, which impacts the predicted convective heat flux. However, LAURA calculations in which the wall temperature was specified to match the estimated surface temperature at the thermal plug locations resulted in only a minor difference in convective heat flux. The HARA prediction of radiative heat flux is shown separately and is not impacted by whether the boundary layer is laminar or turbulent.

Overall, the LAURA/HARA calculations predict that all thermal plug locations experienced higher convective heat flux compared to radiative, as expected, especially after BLT. At all locations, the time of predicted peak total heat flux precedes the time of maximum radiative heat flux, which occurs several seconds later and is suspected to be the cause of a mild secondary bump in some of the reconstructed heating curves near 100 seconds. The laminar calculations predict somewhat higher total heat flux than was reconstructed prior to BLT, when the magnitudes are relatively low. The entire MTH01 and MTH11 heating curves are well predicted with laminar-based total heating because BLT was not detected at these locations near the stagnation point; although, the turbulent LAURA calculations at MTH11 do show a minor increase in convective heating compared to the laminar results. During the times after BLT, the turbulent calculations using the Cebeci-Smith algebraic model produce lower peak heat flux values than the reconstruction. However, the predictions for which locations would see the highest total heating (MTH02 and MTH04) and lowest (MTH01 and MTH11) were confirmed by the data. When only a total heat flux can be reconstructed from the temperature data, it is difficult to pinpoint the root cause of differences between the smooth-wall CFD predictions and data. A number of causes of the differences are possible, but were not (and likely cannot be) measured: surface catalysis different from what was modeled, TPS surface roughness from ablated PICA, and gap filler material protrusions in between PICA tiles. Detailed analysis is ongoing to investigate possible reasons for the discrepancies.

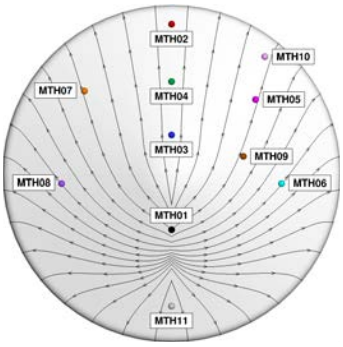

(a) Measurement locations and representative surface streamlines

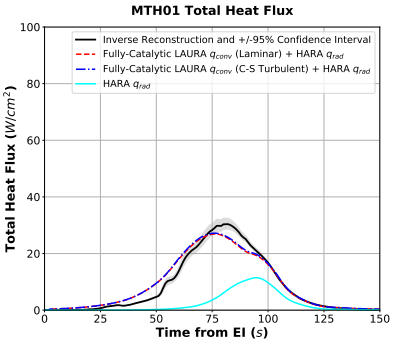

(b) MTH01

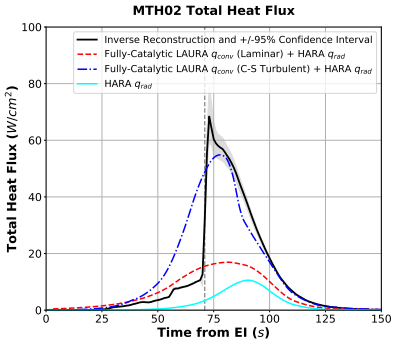

(c) MTH02

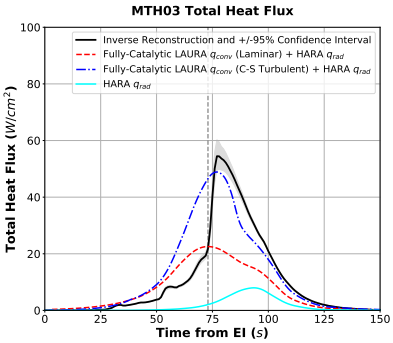

(d) MTH03

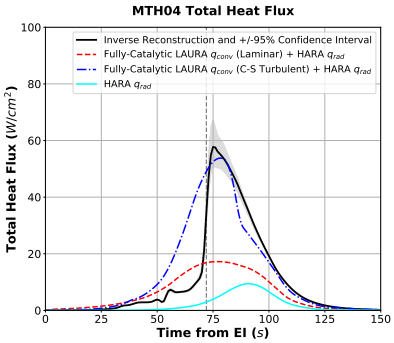

(e) MTH04

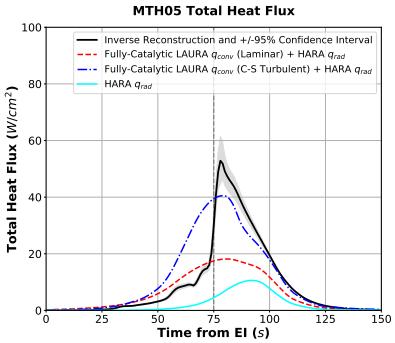

(f) MTH05

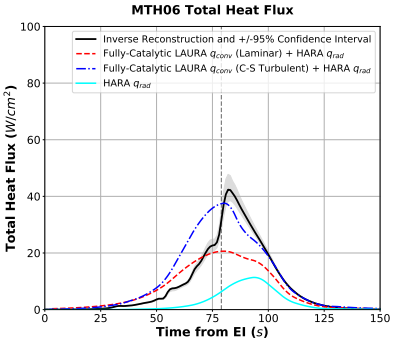

(g) MTH06

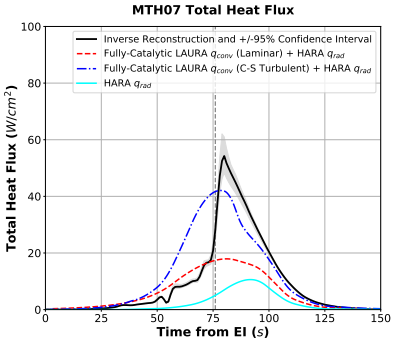

(h) MTH07

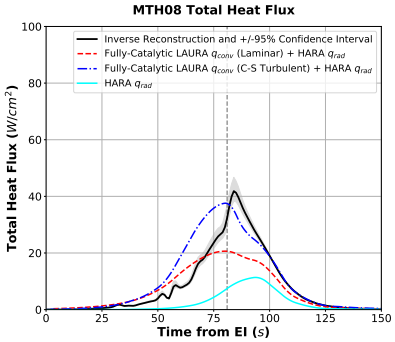

(i) MTH08

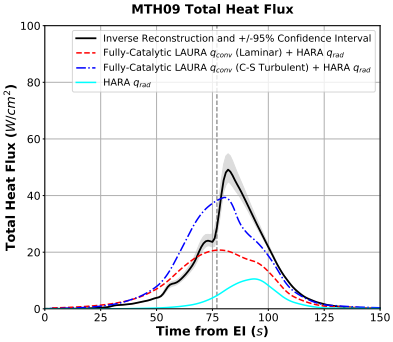

(j) MTH09

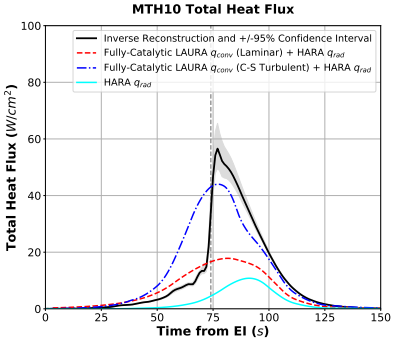

(k) MTH10

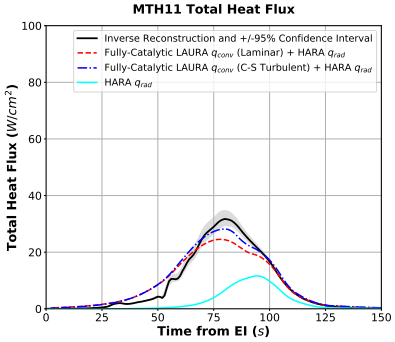

(l) MTH11

Figure 15. Reconstructed heatshield total heat fluxes compared to LAURA/HARA results. BLT is indicated by vertical dashed lines.

LAURA pre-launch calculations used for TPS margin assessments were based on the Baldwin-Lomax algebraic turbulence model and a super-catalytic surface, which maximizes convective heat flux due to full recombination of CO_2. The convective heat flux uncertainty also included turbulent augmentation due to surface roughness. There were no efforts to reduce the design environments uncertainties for Mars 2020 since the heatshield TPS thickness was fixed. Thus, the pre-flight analysis was focused on determining whether the thickness was sufficient to keep the bondline temperature below the maximum allowed. Figure 16 shows the reconstructed heat fluxes compared to the design turbulent convective plus radiative heat flux from the 19-TPS-01 LAURA/HARA calculations, with and without uncertainties. The results are shown for the MTH01 location in the stagnation area, where turbulence was not expected nor observed, and the MTH02 near the location of predicted maximum turbulent heat flux. The 19-TPS-01 trajectory was selected as the shallow entry design trajectory for pre-flight analysis. A steeper 19-TPS-02 trajectory also was analyzed because it resulted in slightly higher heat fluxes. At both locations, the 19-TPS-01 smooth-wall results from LAURA/HARA without any uncertainties are higher than the reconstructed heating. This result is largely due to the 19-TPS-01 trajectory's higher entry speed and the super-catalytic wall assumption. The MTH02 turbulent design heating also includes roughness augmentation of the convective heat flux, but it is impossible to determine from the flight data how much of an effect surface roughness had on the heating.

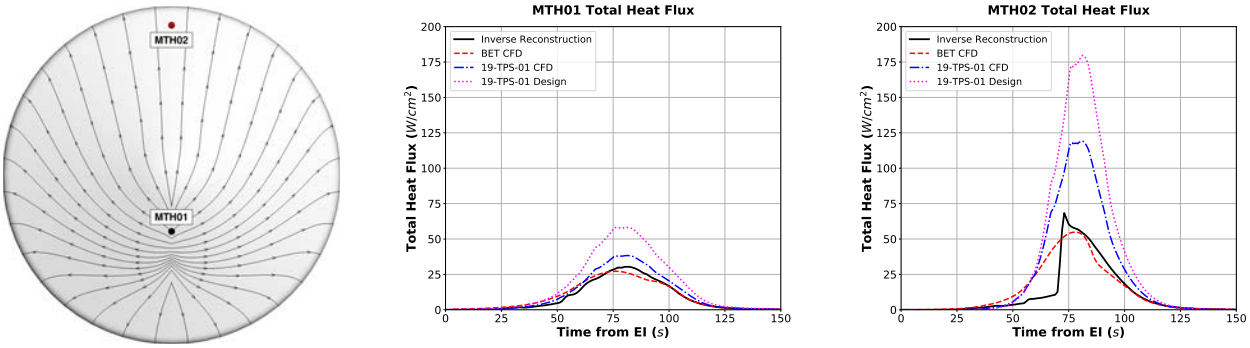

(a) Measurement locations and representative surface streamlines

(b) MTH01

(c) MTH02

Figure 16. Reconstructed heatshield total heat fluxes compared to 19-TPS-01 design trajectory environments and estimated BET design environments at MTH01 and MTH02.

The measured backshell pressure and LAURA prediction at MTB01 is shown in Figure 17. The LAURA laminar results shown are time-averaged from unsteady calculations, as was done for pre-flight analysis. The LAURA curve qualitatively matches the observed timing of peak pressure, but the predicted magnitudes are lower than measured. Unsteady laminar calculations are not the preferred method for predicting unsteady wake flowfields, so further analysis will include detached eddy simulations with more advanced turbulence models.

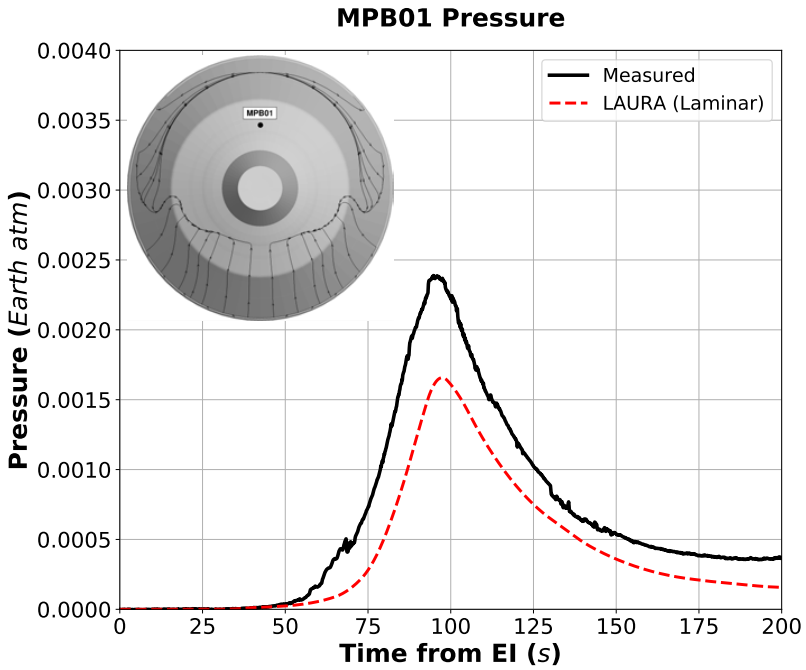

Figure 17. Measured backshell pressure compared to LAURA laminar results.

The reconstructed backshell heating compared to LAURA/HARA analysis is shown in Figure 18. The predicted peak convective plus radiative heating exceeds the reconstructed values at all locations. In some cases, the peak HARA radiative heat flux alone exceeds the total reconstructed heating. At all locations, even in areas where attached flow was expected, the predicted radiative heating makes up the vast majority of the total heating. The CFD calculations qualitatively match the order of maximum to minimum total surface heating among the locations shown. There is no obvious evidence that interference heating from reaction control system thrusters impacted the environments at any of the thermal plug locations, but this remains a topic of research. Additional flowfield calculations with more advanced unsteady turbulence modeling approaches are planned as part of the long-term analysis of the flight data.

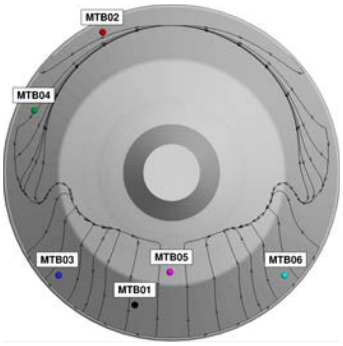

(a) Measurement locations and representative surface streamlines

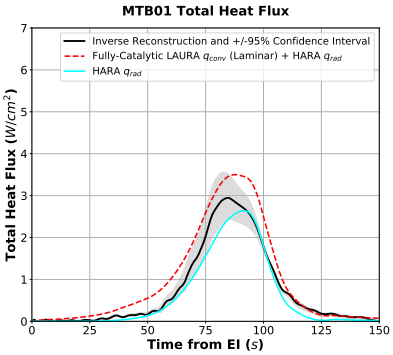

(b) MTB01

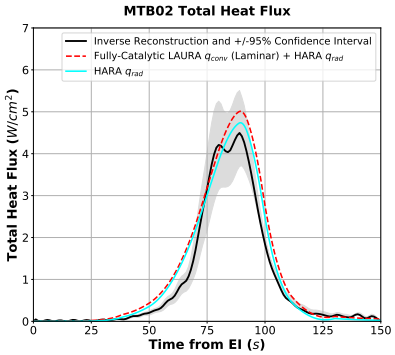

(c) MTB02

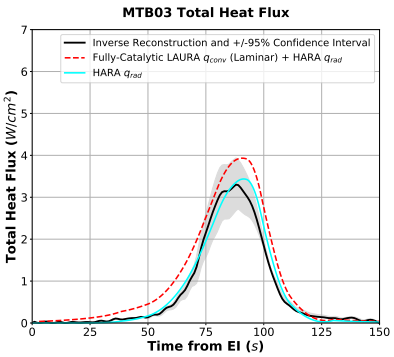

(d) MTB03

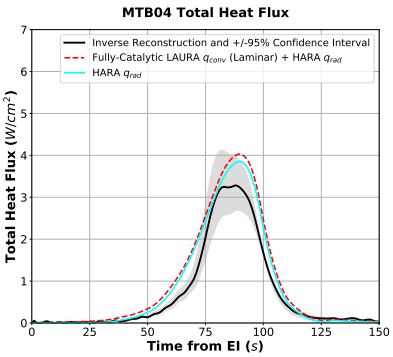

(e) MTB04

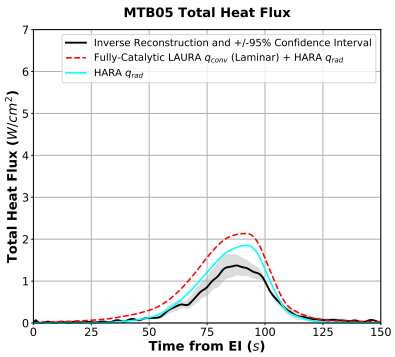

(f) MTB05

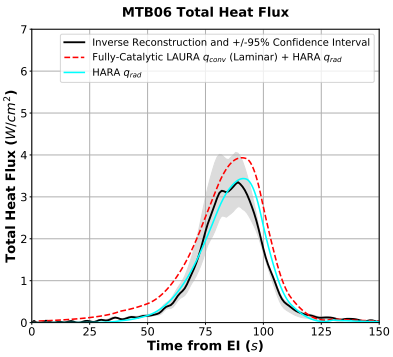

(g) MTB06

Figure 18. Reconstructed backshell total heat fluxes compared to LAURA/HARA results.

The reconstructed and predicted heat fluxes at MTB01 and MTB02 are compared to pre-flight analysis in Figure 19. As was the case for the heatshield, the 19-TPS-01 maximum heating calculated with LAURA and HARA are higher than the BET predicted environments. However, the difference is smaller than it is for the heatshield. Thus, for the backshell aeroheating environments, the 19-TPS-01 entry trajectory was not as conservative for design as it was for the heatshield, even with the higher entry speed and super-catalytic surface boundary condition. Experience from previous analysis suggests that the backshell heating trends in the same direction as freestream dynamic pressure, and since the 19-TPS-01 and BET dynamic pressures are similar (see Figure 11), the backshell aeroheating is as well.

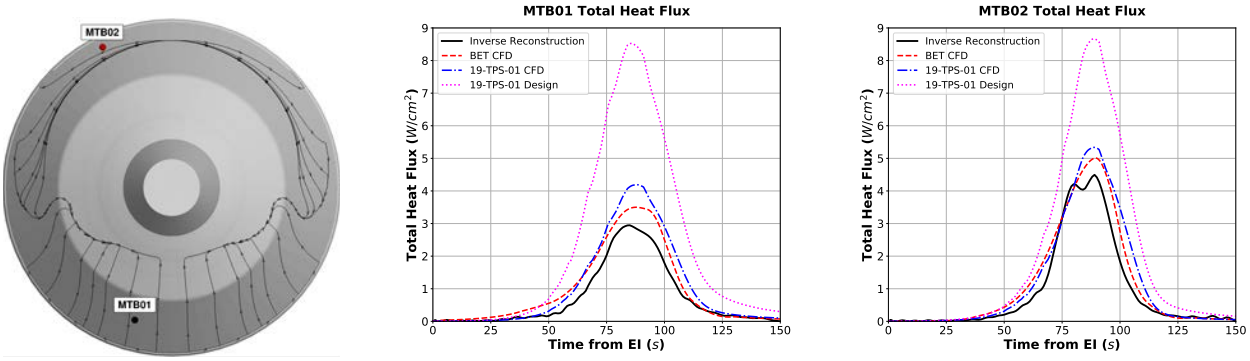

(a) Measurement locations and representative surface streamlines

(b) MTB01

(c) MTB02

Figure 19. Reconstructed backshell total heat fluxes compared to 19-TPS-01 design trajectory environments at MTB01 and MTB02.

VII. Summary and Conclusions

The successful landing of the Mars 2020 Perseverance rover included a suite of engineering data on the entry system aeroshell designed to improve predictive modeling capabilities: surface pressure measurements at six heatshield and one backshell locations, and temperature measurements inside the thermal protection system materials at eleven heatshield and six backshell locations. All sensors successfully returned a complete set of data spanning the entire duration of the aeroshell's flight through the Mars atmosphere prior to landing. The full-range heatshield stagnation pressure and six other pressure measurements that were tuned to lower magnitudes were used to reconstruct the entry trajectory, aerodynamics, and atmospheric density. The temperatures measured inside the thermal protection materials, PICA on the heatshield and SLA-561V on the backshell, were used in combination with thermal response analytical models to back out the total aerodynamic heating at the outer material surface. The temperature measurements closest to the heatshield surface (depths of 1.905 to 2.54 mm) survived the entire entry sequence, indicating that ablative recession never reached those depths. The maximum heatshield temperatures occurred near the leeside shoulder where turbulent conditions were expected away from the stagnation area. The reconstructed total heating (convective plus radiative) showed that boundary layer transition to turbulent conditions occurred at nine of the eleven heatshield measurement locations 71 to 81 seconds after the entry sequence started. Prior to boundary layer transition, the maximum temperatures and heat fluxes occurred at the two heatshield measurement locations in the stagnation area. At the locations where boundary layer transition happened, the maximum total heat flux occurred under turbulent conditions. Among the eleven heatshield measurement locations, maximum total heating occurred near the shoulder where the peak pre-flight heating was expected to occur. At the six backshell locations where temperatures were measured inside the thermal protection material, the total heat flux was reconstructed in a fashion similar to the heatshield. The highest temperatures and total heat flux occurred away from the area of the backshell where attached flow was predicted.

Computational fluid dynamics analysis using the pre-flight design tools was completed on the as-flown trajectory so that results could be compared to measured pressures and reconstructed heat fluxes. The new predictions were obtained on a smooth-wall computational grid that did not include any blowing, surface roughness from ablative material recession, nor discontinuities between PICA tiles. On the heatshield, the predicted peak surface pressure at the stagnation point is within 3% of the measured value. The laminar convective plus radiative heating predictions qualitatively match the as-flown heating at the two stagnation area measurement locations. At the remaining locations where boundary layer transition occurred, the predicted maximum heating based on algebraic turbulence modeling are qualitatively similar to the reconstructed heating, with slightly lower predicted magnitudes. The order of measurement locations with highest to lowest reconstructed heat flux is matched by the predictions. On the backshell, the laminar predictions qualitatively capture the reconstructed heat fluxes, as well as the heat flux magnitude order among the six measurement locations. The predicted heating mostly comes from radiation, even in areas of attached

flow. The pre-flight aeroheating design environments for both the heatshield and backshell are significantly higher than the reconstructed heating. For the heatshield, this result is partly due to the use of the maximum surface catalysis contribution to convective heating and augmented heating from surface roughness. In addition, the pre-flight heatshield analysis was based on a trajectory with a higher entry speed than the entry vehicle actually experienced, resulting in higher convective heating. The backshell aeroheating design environments similarly are much higher than was reconstructed mostly because of conservative convective heating uncertainties. Overall, the post-analysis to date has improved confidence in the pre-flight design tools and methods for Mars entry aeroheating. Additional detailed investigations of all Mars 2020 data products and more in-depth flowfield analysis is forthcoming.

Acknowledgments

The author wishes to thank Adam Wise at NASA Langley Research Center for generating computational grids for Laura/Hara analysis.

References

[1]M. Gazarik, e. a., "Overview of the MEDLI Project," IEEE Paper 2008-1510, IEEE Aerospace Conference, March 2008.

[2]Bose, D., White, T. R., Mahzari, M., and Edquist, K. T., "Reconstruction of Aerothermal Environment and Heat Shield Response of Mars Science Laboratory," *Journal of Spacecraft of Rockets*, Vol. 51, No. 4, July-August 2014, pp. 1174–1184.

[3]Wise, A. J., Prabhu, D. K., Saunders, D. A., Johnston, C. O., and Edquist, K. T., "Computational Aerothermodynamic Environments for the Mars 2020 Entry Capsule," AIAA Paper 2018-3116, June 2018.

[4]Johnston, C. O., Brandis, A. M., and Sutton, K., "Shock Layer Radiation Modeling and Uncertainty for Mars Entry," AIAA Paper 2012-2866, June 2012.

[5]Edquist, K. T., Hollis, B. R., and Johnston, C. O., "Mars Science Laboratory Heat Shield Aerothermodynamics: Design and Reconstruction," *Journal of Spacecraft of Rockets*, Vol. 51, No. 4, July-August 2014.

[6]White, T. R., et al, "Mars Entry Instrumentation Flight Data and Mars 2020 Entry Environments," AIAA Paper 2022-XXXX, January 2022.

[7]Karlgaard, C. D., Schoenenberger, M., Dutta, S., and Way, D. W., "Mars Entry, Descent, and Landing Instrumentation 2 Trajectory and Atmosphere Reconstruction," AIAA Paper 2022-XXXX, January 2022.

[8]Dutta, S., Karlgaard, C., Kass, D., Mischna, M., and Villar, G., "Post-flight Analysis of Atmospheric Properties from Mars 2020 Entry, Descent, and Landing," AIAA Paper 2022-XXXX, January 2022.

[9]Schoenenberger, M., Karlgaard, C., Dutta, S., and Norman, J. W. V., "Assessment of the Reconstructed Aerodynamics of the Mars 2020 Entry Vehicle," AIAA Paper 2022-XXXX, January 2022.

[10]Way, D. W., Dutta, S., Zumwalt, C. H., and Blette, D. J., "Assessment of the Mars 2020 Entry, Descent, and Landing Simulation," AIAA Paper 2022-XXXX, January 2022.

[11]Monk, J., Feldman, J. D., Mahzari, M., White, T. R., Prabhu, D. K., and Alpert, H., "MEDLI2: Ablator Models for Flight," AIAA Paper 2022-XXXX, NASA Ames Research Center, January 2022.

[12]Alpert, H., Mahzari, M., Saunders, D., Monk, J., and White, T. R., "Inverse Estimation of Mars2020 Entry Aeroheating Environments Using MEDLI2 Flight Data," AIAA Paper 2022-XXXX, NASA Ames Research Center, January 2022.

[13]Miller, R. A., Tang, C. Y., White, T. R., and Cruden, B. R., "MEDLI2: MISP Measured Aftbody Aerothermal Environments," AIAA Paper 2022-XXXX, NASA Ames Research Center, January 2022.

[14]Tang, C. Y., Mahzari, M., Prabhu, D. K., Alpert, H., and Cruden, B. R., "MEDLI2: MISP Inferred Aerothermal Environment and Flow Transition Assessment," AIAA Paper 2022-XXXX, NASA Ames Research Center, January 2022.

[15]Chen, Y.-K. and Milos, F. S., "Multidimensional Finite Volume Fully Implicit Ablation and Thermal Response Code," *Journal of Spacecraft and Rockets*, Vol. 55, No. 4, July-August 2018, pp. 914–927.

[16]Mahzari, M., Braun, R. D., and White, T. R., "Reconstruction of Mars Pathfinder Aerothermal Heating and Heatshield Material Response Using Inverse Methods," AIAA Paper 2012-2872, Georgia Institute of Technology, June 2012.

[17]West, T. K. and Brandis, A. M., "Updated Stagnation Point Aeroheating Correlations for Mars Entry," AIAA Paper 2018-3767, June 2018.

[18]Mazaheri, A., Gnoffo, P. A., Johnston, C. O., and Kleb, B., "LAURA Users Manual: 5.5-65135," NASA TM 2013-217800, NASA Langley Research Center, February 2013.

[19]Johnston, C. O. and Brandis, A. M., "Modeling of Nonequilibrium CO Fourth-Positive and CN Violet Emission in CO2-N2 Gases," *Journal of Quantitative Spectroscopy and Radiative Transfer*, Vol. 149, Nov. 2014, pp. 303–317.

[20]Mitcheltree, R. A. and Gnoffo, P. A., "Wake Flow about the Mars Pathfinder Entry Vehicle," *Journal of Spacecraft and Rockets*, Vol. 32, No. 5, Sept-Oct 1995, pp. 771–776.

[21]Mazaheri, A., Johnston, C. O., and Sefidbakht, S., "Three-Dimensional Radiation Ray-Tracing for Shock-Layer Radiative Heating Simulations," *Journal of Spacecraft of Rockets*, Vol. 50, No. 3, May-June 2013, pp. 485–493.